

Convectively Generated Negative Potential Vorticity Enhancing the Jet Stream through an Inverse Energy Cascade during the Extratropical Transition of Hurricane Irma[©]

KEVIN C. PRINCE^a AND CLARK EVANS^a

^a Atmospheric Science Program, University of Wisconsin–Milwaukee, Milwaukee, Wisconsin

(Manuscript received 21 April 2022, in final form 11 July 2022)

ABSTRACT: A tropical cyclone (TC) that recurses into the midlatitudes can lead to significant downstream flow amplification by way of a favorable interaction with the midlatitude waveguide. Current conceptualizations emphasize the role of the meso- α - to synoptic-scale diabatically enhanced vertical redistribution of potential vorticity in facilitating downstream flow amplification following the interaction of a TC with the midlatitude waveguide. Less understood, however, is the extent to which this downstream flow amplification may be facilitated by the convective-scale diabatically enhanced horizontal redistribution of potential vorticity. Consequently, this study aims to diagnose the role that deep, moist convection in an associated predecessor rain event north of the TC played in influencing the midlatitude waveguide and potentially the downstream evolution. A convection-allowing numerical simulation is performed on a predecessor rain event that precedes the interaction of North Atlantic TC Irma in September 2017 with the midlatitude waveguide. Horizontal gradients in microphysical heating result in intense convective-scale potential vorticity dipoles aligned perpendicular to the vertical wind shear vector, with the negative anomaly poleward (and thus closer to the midlatitude waveguide) of the large-scale southwesterly vertical wind shear vector. Regions of intensely negative potential vorticity persist for multiple hours after their formation as they become deformed by the large-scale strain field that is aligned parallel to the background vertical wind shear vector. The deformation-driven thinning of the negative potential vorticity is associated with a transfer of energy to the large-scale flow, suggesting a nonnegligible impact to the TC–midlatitude waveguide interaction by the collection of convective cells embedded in the predecessor rain event.

KEYWORDS: Energy transport; Atmospheric waves; Mesoscale models

1. Introduction

The recurvature of a TC from the tropics or subtropics into the midlatitudes may lead to highly amplified midlatitude waveguide patterns locally and downstream from the recurring TC due to interaction between the TC and an upstream midlatitude trough (Archambault et al. 2013, 2015; Torn and Hakim 2015; Quinting and Jones 2016). In a TC–trough interaction, strong latent heat release inside of the TC leads to the vertical redistribution of low potential vorticity (PV) air into the upper troposphere. When the interaction is favorable, the TC recurses east of upstream trough, in which the low-PV air in the core of the TC is then diabatically enhanced radially away from the TC's core by the TC's secondary circulation against the eastern flank of an upstream midlatitude trough. This advection of near-zero-PV air tightens the local PV gradient on the east side of the trough, leading to local jet streak formation and subsequent downstream impacts that can last for several days (Archambault et al. 2013, 2015; Grams and Archambault 2016; Grams et al. 2011, 2013a,b). Outcomes of TC–trough interactions depend on the inertial stability of the jet (as dictated by the jet speed and latitude), the shape and

phase speed of the upstream trough, the magnitude of the TC's outflow, and the phasing of the TC with the upstream trough (Finocchio and Doyle 2019; Komaromi and Doyle 2018; Riboldi et al. 2019; Riemer and Jones 2014). The impacts from TC–trough interactions can extend several thousand kilometers downstream, with recent downstream high-impact weather such as indirect TC interactions, leading to poor TC intensity and track forecasts (Prince and Evans 2020), high-impact precipitation events (Pohorsky et al. 2019), blocking anticyclones (Riboldi et al. 2019), and the formation of PV streamers, leading to TC formation (Keller 2017; Quinting and Jones 2016; Riemer et al. 2008; Riemer and Jones 2010), being attributed to upstream TC–trough interactions.

Interactions between TCs and the midlatitude waveguide may be occasionally accompanied by preconditioning, which are processes that establish an extratropical environment that supports baroclinic development (Grams and Archambault 2016; Keller et al. 2019). Preconditioning is often manifest in the form of a predecessor rain event (PRE), a meso- α feature composed of individual convective cells embedded in a larger stratiform region of high-impact heavy rainfall well in advance of a recurring TC (Bosart et al. 2012; Cordeira et al. 2013; Cote 2007; Galarneau et al. 2010; Galarneau 2015). Warm, moist air advected poleward by a TC's outer circulation impinges upon a baroclinic zone 500–2000 km away (Bosart and Carr 1978; Moore et al. 2013), whereupon it ascends and generates a broad region of stratiform precipitation with embedded deep, moist convection. The vertical gradient of diabatic heating in both deep, moist convection and

[©] Supplemental information related to this paper is available at the Journals Online website: <https://doi.org/10.1175/JAS-D-22-0094.s1>.

Corresponding author: Kevin Prince, kprince@uwm.edu

stratiform precipitation reduces upper-tropospheric potential vorticity (PV) through vertical redistribution. Diabatically enhanced divergent outflow above the PRE radially advects this low-PV air away from the PRE near the tropopause (Archambault et al. 2013; Grams and Archambault 2016; Keller et al. 2019). This diabatically enhanced negative PV advection aloft associated with convective and stratiform precipitation inside of the PRE is analogous to the diabatically enhanced negative PV advection aloft by a TC's secondary circulation (Archambault et al. 2013). The diabatic processes in the PRE can also assist with anchoring and meridional amplification of the midlatitude jet primarily in the vicinity of the downstream ridge and can promote a "synergistic interaction" with the midlatitude waveguide (Bosart and Lackmann 1995; Evans et al. 2017; Grams et al. 2011; Archambault et al. 2015; Grams and Archambault 2016; Keller et al. 2019; Riboldi et al. 2019).

On synoptic scales, it is often assumed that vertical diabatic-heating gradients are the primary contributors to isentropic PV non-conservation following the motion, with horizontal diabatic-heating gradients having a secondary, often negligible contribution. Consequently, the PV tendency equation along an isentropic surface is often written as follows:

$$\frac{D}{Dt} \text{PV} \approx \frac{1}{\sigma} (\zeta + f) \frac{\partial \dot{\theta}}{\partial p}, \quad (1)$$

where $\sigma = -(1/g)(\partial p / \partial \theta)$, ζ is the relative vorticity, p is pressure, $\dot{\theta}$ is the diabatic warming rate, θ is potential temperature, g is gravity, and f is the Coriolis parameter. However, (1) does not hold in the presence of strong horizontal diabatic-heating gradients, such as those found with individual convective cells.

On convective scales, deep, moist convection in a vertically sheared background flow can generate PV with values an order of magnitude larger than typical synoptic-scale PV (Chagnon and Gray 2009; Oertel et al. 2020). In a PV framework, this is represented by intense horizontal gradients of diabatic warming $\dot{\theta}$ (Chagnon and Gray 2009), which are not represented in (1) and require the fully three-dimensional form written as follows:

$$\frac{D}{Dt} \text{PV} = -\frac{1}{\sigma} [(\nabla_{\theta} \times \mathbf{v}_{\theta} + f \mathbf{k}) \cdot \nabla_{\theta} \dot{\theta}], \quad (2)$$

where $\mathbf{v}_{\theta} = (u, v, \dot{\theta})$ represents the three-dimensional wind on an isentropic surface, $\nabla_{\theta} = (\partial_x, \partial_y, \partial_{\theta})$ represents the three-dimensional gradient operator on an isentropic surface, and $\mathbf{k} = (0, 0, 1)$ represents the unit vector perpendicular to an isentropic surface.

This process is analogous to the tilting of horizontal vorticity into the vertical by a localized updraft that produces cyclonic and anticyclonic curvature straddling the updraft (e.g., Davies-Jones 1986). The structure of these anomalies is dictated by the direction of the vertical wind shear vector, with negative PV resulting to the left of the deep-layer vertical wind shear vector and positive PV resulting to the right of the deep-layer vertical wind shear vector (Oertel et al. 2020). Given a primarily westerly background vertical wind shear vector in the midlatitudes, convection inside of a PRE

equatorward of the midlatitude waveguide between the jet and a recurving TC (Harvey et al. 2020), would produce convective-scale strongly negative PV poleward of the convective cell, against the waveguide (see Fig. 1 of Oertel et al. 2020).

While the PV produced by a single convective cell are small in scale and individually insignificant on the synoptic scales, a collection of organized convective cells may cause a meaningful impact to the large-scale flow by opposing the background horizontal flow and generating a distinct negative anomaly in wind speed (Oertel and Schemm 2021). However, whether these impacts are meaningful on the meso- α to synoptic scales has yet to be determined. Energy in large-scale turbulence is generally thought to cascade into progressively smaller eddies, eventually reaching the Kolmogorov scale where viscosity dominates, and turbulent kinetic energy is dissipated into heat (Pope 2000). In some cases, however, an inverse energy cascade (Kraichnan 1967) may transfer energy from smaller to larger scales (Eyink 2006a,b; Chen et al. 2006; Xiao et al. 2009). In this context, small-scale features add energy to the large-scale flow, which has been hypothesized to be supported by a "thinning" of small-scale vorticity anomalies by the large-scale flow; however, the physical mechanism by which this inverse cascade is accomplished is an ongoing discussion.

This study tests the hypothesis that deep, moist convection associated with a PRE modified the synoptic-scale midlatitude waveguide in a recent TC-midlatitude waveguide interaction by way of the production of convective-scale intensely negative PV against the waveguide by deep, moist convection. A convection-allowing simulation of the PRE in advance of North Atlantic TC Irma (2017)'s interaction with the midlatitude waveguide is performed to test this hypothesis. The paper is organized as follows. A case overview, simulation configuration details, and analysis procedures are described in section 2. The simulation is verified in section 3. Section 4 diagnoses the physical mechanisms which produce and maintain the convective-scale PV anomalies. Section 5 investigates the transfer of energy in the vicinity of the PRE and the physical mechanisms which lead to these transfers of energy. A summary and discussion are provided in section 6.

2. Methods

a. Case overview

The PRE associated with North Atlantic TC Irma in September 2017 (Fig. 1), which caused approximately \$50 billion in damage in Florida (NHC 2018), is selected for study. TC Irma's interaction with an upstream midlatitude trough following the PRE amplified the initial downstream anticyclone, which in turn influenced the track and intensity of the downstream TC Jose (Prince and Evans 2020).

At 1200 UTC 10 September 2017, TC Irma is located in the Florida Straits (Fig. 1, denoted by I) downstream of a midlatitude trough over the southeastern United States (Fig. 1). A PRE is located along the southeast U.S. coastline, poleward of TC Irma and eastward of the midlatitude trough (Figs. 1; Figs. S1 and S2 in the online supplemental material; denoted by P). Upper-tropospheric outflow associated with the PRE

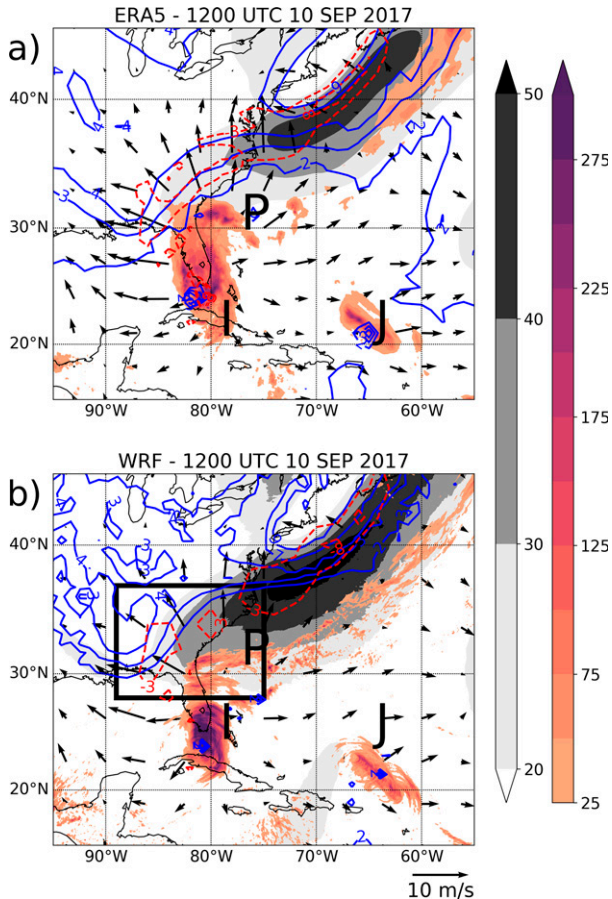


FIG. 1. The 250–150-hPa layer-mean PV (blue contours at 2, 3, 4, 7, and 9 PVU, where $1 \text{ PVU} = 1 \times 10^{-6} \text{ K kg}^{-1} \text{ m}^2 \text{ s}^{-1}$), 250–150-hPa layer-mean horizontal wind speed (gray shading in m s^{-1} per the color bar at right), 250–150-hPa layer-mean irrotational wind (vectors; m s^{-1} ; reference vector at lower right), horizontal advection of the 250–150-hPa layer-mean potential vorticity by the 250–150-hPa layer-mean irrotational wind (red dashed contours at -8 and -3 PVU day^{-1}), and 24-h (0000–2359 UTC 10 Sep) accumulated precipitation (color shading; in mm per the color bar at right) at 1200 UTC 10 Sep 2017. (a) From the ERA5 (Hersbach et al. 2020) for 24-h accumulated precipitation, which is obtained from the $0.1^\circ \times 0.1^\circ$ NASA Integrated Multi-satellitE Retrievals for GPM (IMERG; Huffman et al. 2019) version 06 dataset, and (b) from the numerical simulation performed in this study (described below). TC Irma, TC Jose, and the PRE are indicated by the boldface letters I, J, and P, respectively. The black box in (b) denotes the region over which all area averages are performed in this study.

and TC Irma's outer rainbands is impinging upon the upstream trough's eastern flank, as characterized by upper-tropospheric negative PV advection by the irrotational wind (Fig. 1), which subsequently strengthens the upper-tropospheric PV gradient on the trough's eastern flank. Following this time, TC Irma favorably interacts with the upstream trough, amplifying the downstream flow, trapping TC Jose equatorward of the downstream upper-tropospheric anticyclone within a high-shear environment (Prince and Evans 2020).

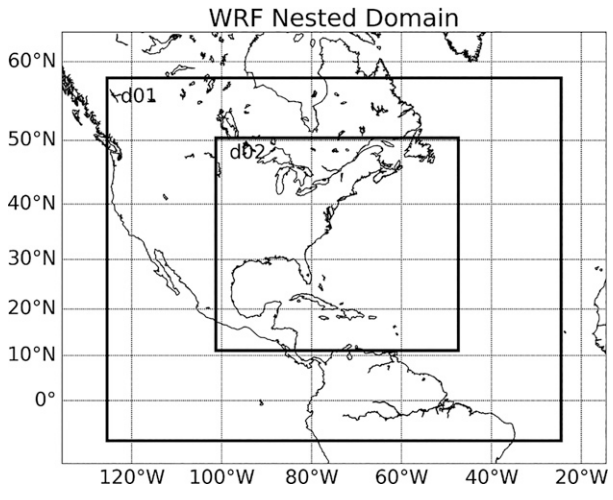


FIG. 2. Simulation domains.

b. Simulation configuration

A single numerical simulation is performed using the Advanced Research version of the Weather Research and Forecasting Model (WRF-ARW), version 4.0 (Skamarock et al. 2019). The WRF-ARW is a fully compressible, nonhydrostatic numerical model. A doubly nested domain is utilized, with the outer domain containing 1000×1250 horizontal grid points at a grid spacing of 9 km and the inner domain containing 1753×2002 horizontal grid points at a grid spacing of 3 km (Fig. 2). Both domains contain 50 terrain-following (σ) vertical levels, including seven vertical levels near the tropopause ($0.15 \leq \sigma \leq 0.25$). The simulation extends 180 h from 0000 UTC 9 September to 1200 UTC 16 September 2017. The initialization time ensures appropriate spinup time of circulations which the initial conditions are unable to represent before the initiation of the PRE (~1200 UTC 9 September 2017). The simulation's long duration allows for verification of the downstream midlatitude evolution following the PRE (and, subsequently, TC Irma) with the upstream trough. Initial and lateral boundary conditions for the model are provided by 6-hourly 0.25° National Centers for Environmental Prediction (NCEP) Global Forecast System (GFS; NCEP 2015). Physical parameterizations are selected following previous TC modeling studies using the WRF-ARW Model (e.g., Torn and Davis 2012; Rios-Berrios et al. 2016). A full list of model configuration parameters is given in Table 1.

c. PV tendency equation in isentropic coordinates

The three-dimensional PV tendency equation on an isentropic surface, including nonhydrostatic effects but excluding friction, non-microphysical diabatic processes (due to the scale of these processes being several orders of magnitude smaller than the microphysical tendency), and contributions from the planetary boundary layer scheme (due to turbulent mixing being small in the midtroposphere/free atmosphere; Attinger et al. 2021) being excluded, is an expanded form of (2) comprised of adiabatic advective and diabatic non-conservative tendencies:

TABLE 1. Model configuration. Unless specified, all parameters apply to both the outer and inner simulation domains.

Model parameter	Selected configuration
Model version	WRF-ARW v4.0 (Skamarock et al. 2019)
Domains	Domain 1 (outer): $1000 \times 1250 \times 50$ levels Domain 2 (inner): $1753 \times 2002 \times 50$ levels
Duration	180 h, 0000 UTC 09 Sep to 1200 UTC 16 Sep 2017
Horizontal grid spacing	Domain 1: 9 km Domain 2: 3 km
Initial and boundary conditions	6-hourly 0.25° GFS operational analyses
Deep cumulus parameterization	Domain 1: New Tiedtke scheme (Zhang and Wang 2017) Domain 2: No parameterization
Microphysical parameterization	WRF single-moment 6-class scheme (Hong et al 2006a)
Boundary layer parameterization	YSU (Hong et al. 2006b)
Surface layer parameterization	Revised MM5 scheme (Jiménez et al. 2012)
Land surface parameterization	Unified Noah Land Surface Model (Tewari et al. 2004)
Longwave radiation parameterization	RRTM scheme (Mlawer et al. 1997)
Shortwave radiation parameterization	Dudhia scheme (Dudhia 1989)

$$\frac{\partial PV}{\partial t} = -\mathbf{v}_\theta \cdot \nabla_\theta PV + PV \frac{\partial \dot{\theta}_{mp}}{\partial \theta} - \frac{1}{\sigma} [(\nabla_\theta \times \mathbf{v}_\theta + f\mathbf{k}) \cdot \nabla_\theta \dot{\theta}_{mp}], \quad (3)$$

where $\dot{\theta}_{mp}$ represents the microphysical diabatic heating (H_DIABATIC in the WRF-ARW Model). In (3), the first right-hand-side term represents the conservative (adiabatic) three-dimensional advection of PV, the second right-hand-side term represents the non-conservative diabatically enhanced vertical redistribution of isentropic potential vorticity, and the third right-hand-side term represents the non-conservative diabatically enhanced horizontal redistribution of potential vorticity. Equation (3) is evaluated using model outputs at 3-min intervals to capture the short-lived nature of the convective elements in the simulation, with partial derivatives approximated utilizing a forward finite difference for time and a fourth-order-accurate centered finite difference for space.

d. Local energy flux and the inverse energy cascade

To diagnose the potential impacts of convective-scale processes on the larger-scale flow, the local energy flux, which can be contextualized as the deformation work performed on small-scale turbulent stress by large-scale strains ([Eyink 2006a,b; Chen et al. 2006; Cai and Mak 1990; Rivièvre and Joly 2006; Xiao et al. 2009](#)), is calculated. The local energy flux is negative when large-scale strains thin smaller-scale turbulent stresses, describing the situation where the larger-scale flow extracts kinetic energy from the turbulent anomalies.

To compute the local energy flux, the filtering approach demonstrated in [Meneveau and Katz \(2000\)](#) is first used to define a “large-scale” ($\overline{\mathbf{u}_{\theta\ell}}$), where $\mathbf{u}_\theta = (u, v)$ is the horizontal wind, and the θ denotes that these calculations were performed on an isentropic surface. In this approach, a “large-scale” velocity field at length scale ℓ is introduced using a low-pass filter:

$$\overline{\mathbf{u}_{\theta\ell}}(x) = \int dr G_\ell(r) \mathbf{u}_\theta(x + r), \quad (4)$$

where x is the spatial location, and r is the radial extent of the window over which the integral is taken. The function defining the window is

$$G_\ell(r) = \frac{1}{\ell^2} G\left(\frac{r}{\ell}\right), \quad (5)$$

where $G_\ell(r)$ can be any Gaussian function with unit integral (sum equal to one). Following [Xiao et al. \(2009\)](#), $G(r)$ is defined as

$$G(r) = \sqrt{\frac{6}{\pi}} \exp(-6r^2), \quad (6)$$

where $G_\ell(r)$ represents a Gaussian convolution filter in physical space. An example of applying (6) with an arbitrary width of 67 grid points (200 km) to the two-dimensional horizontal wind on the 335-K isentropic surface is given in [Fig. 3](#). A Gaussian convolution is selected over other potential convolution filters (such as spectral and box filters) because it is quasi-local in both physical and spectral space ([Xiao et al. 2009](#)), which allows the interpretation of the spatial properties at a particular length scale (ℓ) of the field being filtered. Note that the large-scale $\overline{\mathbf{u}_{\theta\ell}}$ defined above is not identical to a Reynolds-averaged quantity, such that the average of perturbations is not equal to zero ($\overline{\mathbf{u}_{\theta\ell}} \neq 0$).

The local energy flux across a particular length scale ℓ is defined as follows:

$$\Pi_{\theta\ell}(x, t) = -\overline{\mathbf{S}_{\theta\ell}}(x, t) \cdot \boldsymbol{\tau}_{\theta\ell}, \quad (7)$$

where $\overline{\mathbf{S}_{\theta\ell}}$ is the large-scale-strain tensor, given by

$$\overline{\mathbf{S}_{\theta\ell}} = \frac{1}{2} [(\nabla \overline{\mathbf{u}_{\theta\ell}}) + (\nabla \overline{\mathbf{u}_{\theta\ell}})^T], \quad (8)$$

where $\nabla = (\partial_x, \partial_y, 0)$, $\overline{\mathbf{u}_{\theta\ell}}$ is the filtered wind field defined in (4), and $\boldsymbol{\tau}_{\theta\ell}$ is the small-scale stress tensor, given by

$$\boldsymbol{\tau}_{\theta\ell} = (\overline{\mathbf{u}_\theta \mathbf{u}_\theta})_\ell - \overline{\mathbf{u}_{\theta\ell}} \overline{\mathbf{u}_{\theta\ell}}. \quad (9)$$

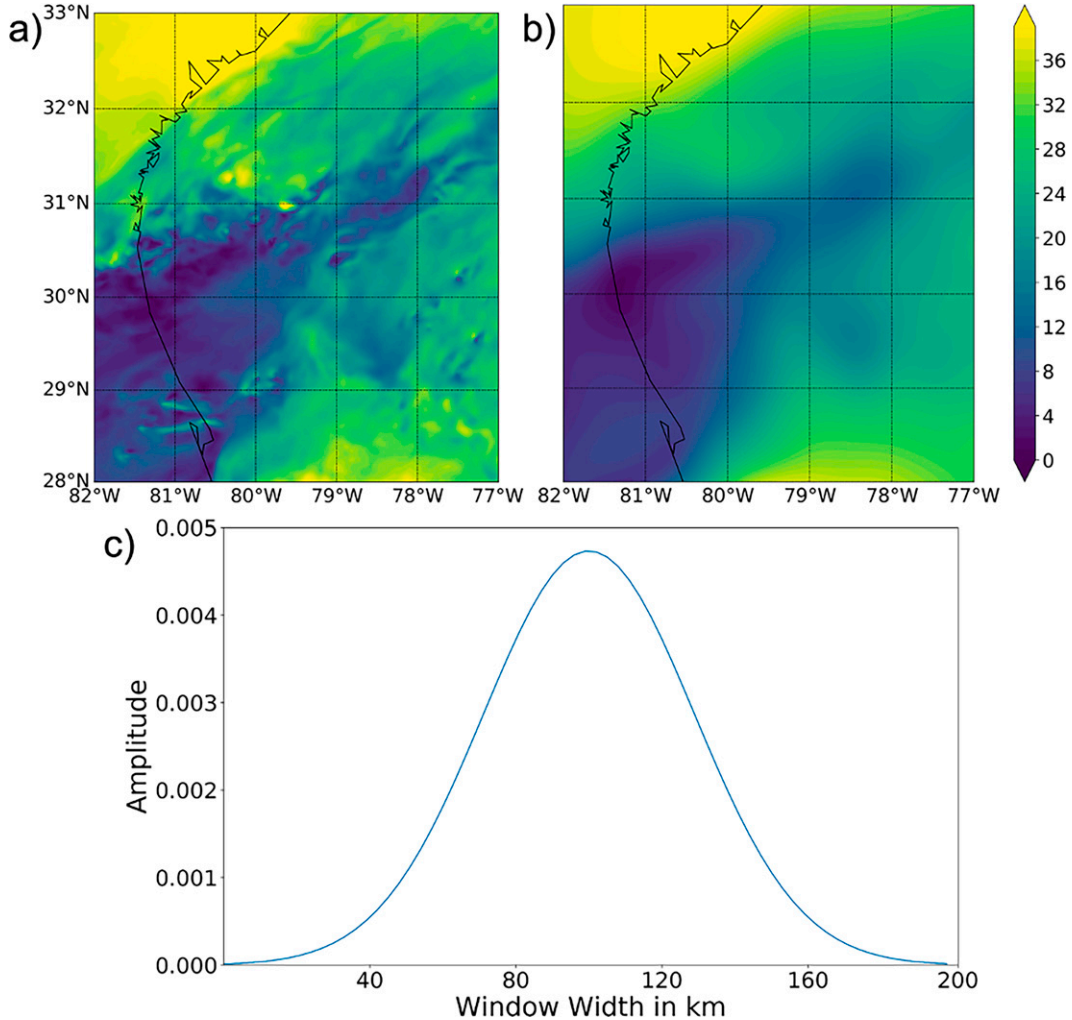


FIG. 3. Horizontal wind speed on the 335-K isentropic surface (shaded in m s^{-1} per the color bar at right) at 0900 UTC 10 Sep 2017 (a) before and (b) after filtering applied by a (c) Gaussian filter with a length scale ℓ of 200 km (width of 67 grid points).

The local energy flux (7) can alternatively be viewed as a deformation work (Eyink 2006a,b; Xiao et al. 2009) done on small-scale turbulent stresses ($\tau_{\theta\ell}$) by the large-scale strain field ($\overline{\mathbf{S}_{\theta\ell}}$). As a reminder, negative deformation work represents the large-scale strain extracting energy from small-scale turbulent stresses, characterizing an inverse cascade of energy from small to large scales, whereas positive deformation work represents the large-scale strain transferring energy to small-scale turbulent stresses. A full derivation of (7) from the filtered two-dimensional Navier-Stokes equations can be found in Xiao et al. (2009).

Although the local energy flux (7) can illustrate the direction of energy transfer in physical space, it is also helpful to evaluate the physical processes that contribute to energy changes in spectral space to view energy transfers more readily across various wavelengths. The spectral kinetic energy budget first introduced by Peng et al. (2014) and applied in Menchaca and Durran (2019) is used to do so. First, the horizontal kinetic energy budget can be defined as follows:

$$\frac{\partial}{\partial t} \text{KE}_h = \mathbf{T}(k) + \mathbf{B}(k) + \mathbf{V}(k) + \mathbf{D}(k), \quad (10)$$

where the subscript of h denotes horizontal, and k denotes the one-dimensional wavenumber. From right to left, the forcing terms of (10) represent the nonlinear advective transfer of energy between wavenumbers (\mathbf{T}), the conversion of available potential energy to horizontal kinetic energy (associated with buoyancy \mathbf{B}), the divergence of the vertical kinetic energy flux (\mathbf{V}), and dissipation (\mathbf{D}). All terms are defined following Menchaca and Durran (2019).

The nonlinear advective transfer term $\mathbf{T}(k)$ is given by

$$\begin{aligned} \mathbf{T}(k) = -\bar{\rho} & \left\{ \left[\mathbf{u} \cdot \nabla \mathbf{u} + \frac{1}{2} \mathbf{u} (\nabla \cdot \mathbf{u}) \right]_k - \frac{1}{2} (\partial_z \mathbf{u}, w \mathbf{u})_k \right. \\ & \left. + \frac{1}{2} (\mathbf{u}, w \partial_z \mathbf{u})_k \right\} + \text{c.c.}, \end{aligned} \quad (11)$$

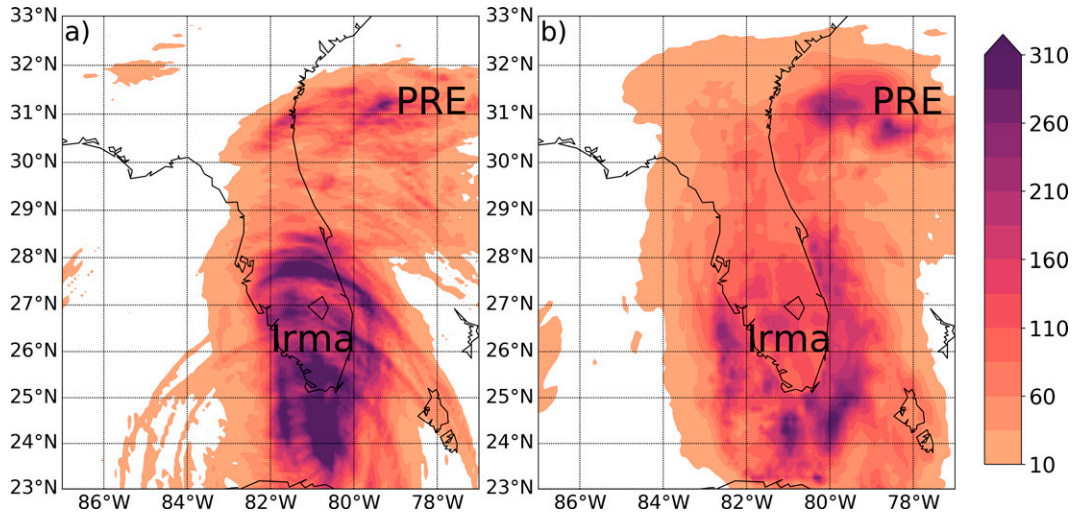


FIG. 4. The 24-h accumulated precipitation (shaded in mm per the color bar at right) between 0000 and 2359 UTC 10 Sep 2017 from the (a) WRF-ARW simulation coarsened to $0.1^\circ \times 0.1^\circ$ horizontal grid spacing and (b) $0.1^\circ \times 0.1^\circ$ NASA IMERG version 06 dataset. The approximate location of the PRE is denoted in both plots.

where ρ is density, $\mathbf{u} = (u, v)$, $\nabla = (\partial_x, \partial_y, 0)$, and c.c. denotes the complex conjugate of the bracketed term. Terms of the form $(\mathbf{a}, \mathbf{b})_k$ can be written as $\hat{\mathbf{a}}^*(k) \cdot \hat{\mathbf{b}}(k)$, where a hat denotes the forward Fourier transform and an asterisk denotes the complex conjugate (Peng et al. 2014; Menchaca and Durran 2019). The overbar on density in (11) and subsequent equations denotes the average over the analysis domain.

The buoyancy forcing term $\mathbf{B}(k)$ is given by

$$\mathbf{B}(k) = c_p \bar{\rho} \bar{\theta}(w, \partial_z \pi')_k + \text{c.c.}, \quad (12)$$

where c_p is the specific heat at constant pressure, θ is the potential temperature, w is the vertical velocity, and π' is the perturbation Exner pressure, where $\bar{\pi} = (\bar{p}/p_0)^{R_d/c_p}$, with \bar{p} being the area-averaged pressure, $p_0 = 1000$ hPa, and $R_d = 287 \text{ J K}^{-1} \text{ kg}^{-1}$.

The divergence of the vertical kinetic energy flux $\mathbf{V}(k)$ is given by

$$\mathbf{V}(k) = -\frac{1}{2} \partial_z [\bar{p}(\mathbf{u}, w\mathbf{u})_k] - c_p \partial_z [\bar{\rho} \bar{\theta}(w, \pi')_k] + \text{c.c.} \quad (13)$$

Finally, the dissipation term $\mathbf{D}(k)$ is calculated as a residual from (10).

All terms are interpolated to height surfaces every 500 m between 5.5 and 17 km above ground level. Layer averages are then performed for the midtroposphere (5.5–9 km), upper troposphere (9.5–13 km), and lower stratosphere (13.5–17 km), which match the layers considered by Menchaca and Durran (2019). Horizontal derivatives are calculated on constant height surfaces and all partial derivatives are approximated utilizing a second-order-accurate centered finite difference. Fourier transforms are performed on one-dimensional zonal splices of data using the fast Fourier transform available in Python's SciPy package (Virtanen et al. 2020), then averaged meridionally over the analysis domain. Given that the simulation (Fig. 2) and analysis (defined in section 5) domains are limited in area, a Tukey

window is applied to the one-dimensional splices of data prior to performing the fast Fourier transform (Bloomfield 2000). This window tapered the data to zero on both ends, which will not remove all artificial noise produced by the decomposition, yet the tapering was selected to be gradual enough to minimize artificial noise produced by drastic gradients in the FFT operation.

To examine energy transfer across wavenumbers, each forcing term in (10) can be expressed in terms of its cumulative sum ($\Pi_{\mathbf{X}}$) over all wavenumbers k (Menchaca and Durran 2019). For any variable $\mathbf{X}(k)$:

$$\Pi_{\mathbf{X}}(k) = \sum_{k \leq l \leq N} \mathbf{X}(l), \quad (14)$$

where N is the maximum one-dimensional wavenumber. In this framework, wavenumbers at which $\Pi_{\mathbf{X}}$ has a negative slope (e.g., higher values at smaller wavenumbers) represent wavenumbers at which $\mathbf{X}(k)$ increases kinetic energy. Conversely, wavenumbers at which $\Pi_{\mathbf{X}}$ has a positive slope (e.g., higher values at larger wavenumbers) represent wavenumbers at which $\mathbf{X}(k)$ decreases kinetic energy. Since $\mathbf{T}(k)$ describes conservative energy transfers between wavenumbers, the sign of $\Pi_{\mathbf{T}}$ indicates whether there is an upscale or downscale cascade of energy. Consequently, positive values of $\Pi_{\mathbf{T}}(k)$ indicate downscale energy transfer to larger wavenumbers whereas negative values of $\Pi_{\mathbf{T}}(k)$ indicate upscale energy transfer to smaller wavenumbers. While we have discussed spectral analyses in terms of wavenumber up to this point, for ease of interpretability and physical understanding, the results in this paper will be presented in a wavelength format. For context, small wavenumbers correspond to large wavelengths, while large wavenumber correspond to small wavelengths.

3. Model verification

Given this study's emphasis on diagnosing the influence of convective-scale diabatically generated PV anomalies on the

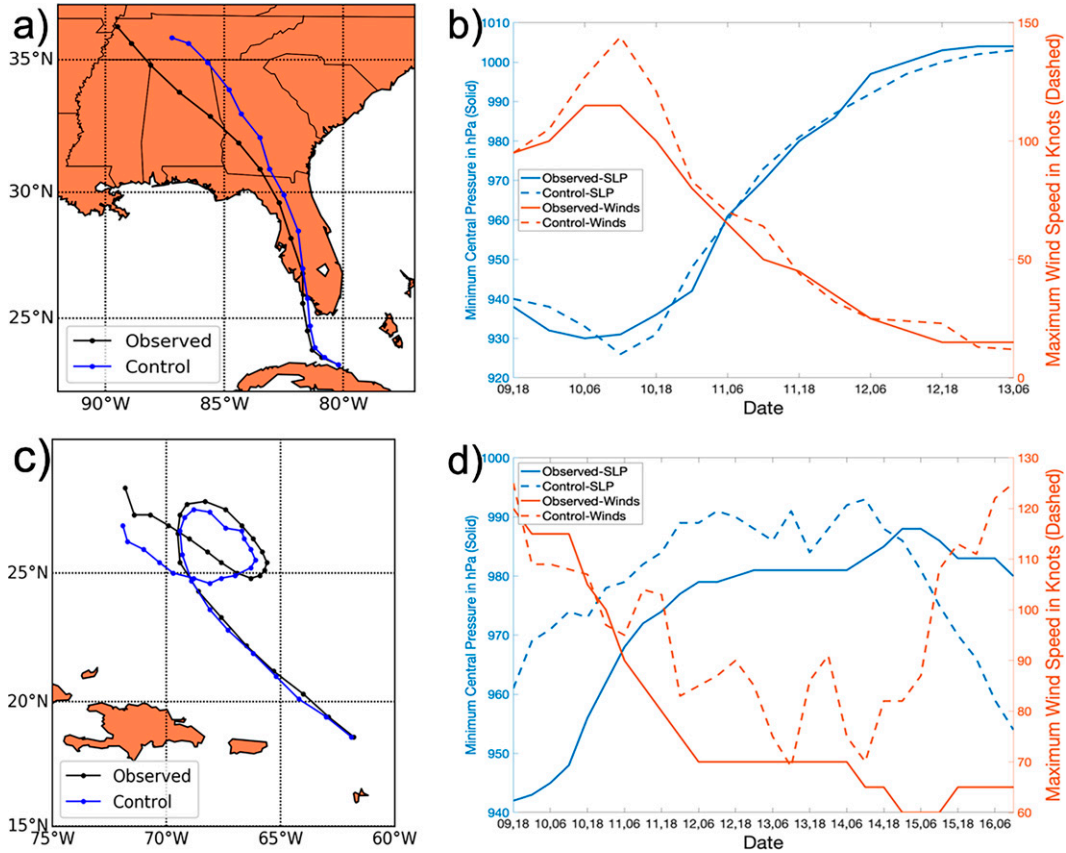


FIG. 5. (a),(c) Simulated (blue lines) and National Hurricane Center best track (black lines) tracks for (a) TC Irma (between 1800 UTC 9 Sep and 0600 UTC 13 Sep 2017, at which time TC Irma was declared post-tropical) and (c) TC Jose (over the simulation's entirety). (b),(d) Simulated (dashed lines) and National Hurricane Center best track (solid lines) minimum sea level pressure (hPa; blue lines) and maximum sustained 10-m wind speed (kt; orange lines) for (b) TC Irma (between 1800 UTC 9 Sep and 0600 UTC 13 Sep 2017, at which time TC Irma was declared post-tropical) and (d) TC Jose (over the simulation's entirety).

midlatitude waveguide, the verification presented herein focuses on diagnosing the extent to which the model simulation accurately predicted rainfall within the PRE and, subsequently, the tracks and intensities of TCs Irma and Jose. TC tracks are primarily dictated by tropospheric-deep mean flow (Velden and Leslie 1991), therefore accurate track (and subsequent intensity) forecasts for the two TCs are indicative of the simulation accurately capturing the large-scale flow pattern in the vicinity of the TCs. Additionally, while we acknowledge that Jose did not play a role in this study, we have elected to include verification data for it, as we hypothesize that the upstream interaction involving the PRE and Irma had an impact to Jose's track and intensity (Prince and Evans 2020).

The interaction between the upstream trough, Irma, and the PRE, appears to be well captured in the simulation, with the placement and strength of the midlatitude jet being well captured 36 h into the simulation (Fig. 1). Positioning of the precipitation inside of the PRE was also well captured by the simulation, with a distinct maximum of precipitation oriented from east to west along the 31°N (Fig. 4). While precipitation

totals were generally well represented in the simulation (mean absolute error of 10 mm over the domain shown in Fig. 4), the heavier precipitation covered a smaller spatial area than observed (Fig. 4), although this may be at least partially due to resolution differences between the two datasets. Given that our study is interested in the amount of diabatic heating occurring in the PRE, the amount of precipitation which fell (vs. positioning the precipitation) is of primary concern, which appears to have been well captured by the simulation (Fig. 4).

The simulation accurately predicts TC Irma's track and intensity (Figs. 5a,b). The TC Irma lifetime average track error is 92 km (compared to the climatological 72-h track forecast error of 191 km; Cangialosi 2018), with a slight east bias following landfall (Fig. 5a), and the TC Irma lifetime average intensity error is 6 kt (3.1 m s^{-1} ; compared to the climatological 72-h intensity forecast error of 12.6 kt (6.5 m s^{-1}); Cangialosi 2018), with the simulated minimum sea level pressure and 10-m wind speeds closely resembling their National Hurricane Center best track values (Fig. 5b). Simulated track and intensity errors for TC Jose are slightly larger (Figs. 5c,d). Both the simulated and observed TCs complete an anticyclonic loop;

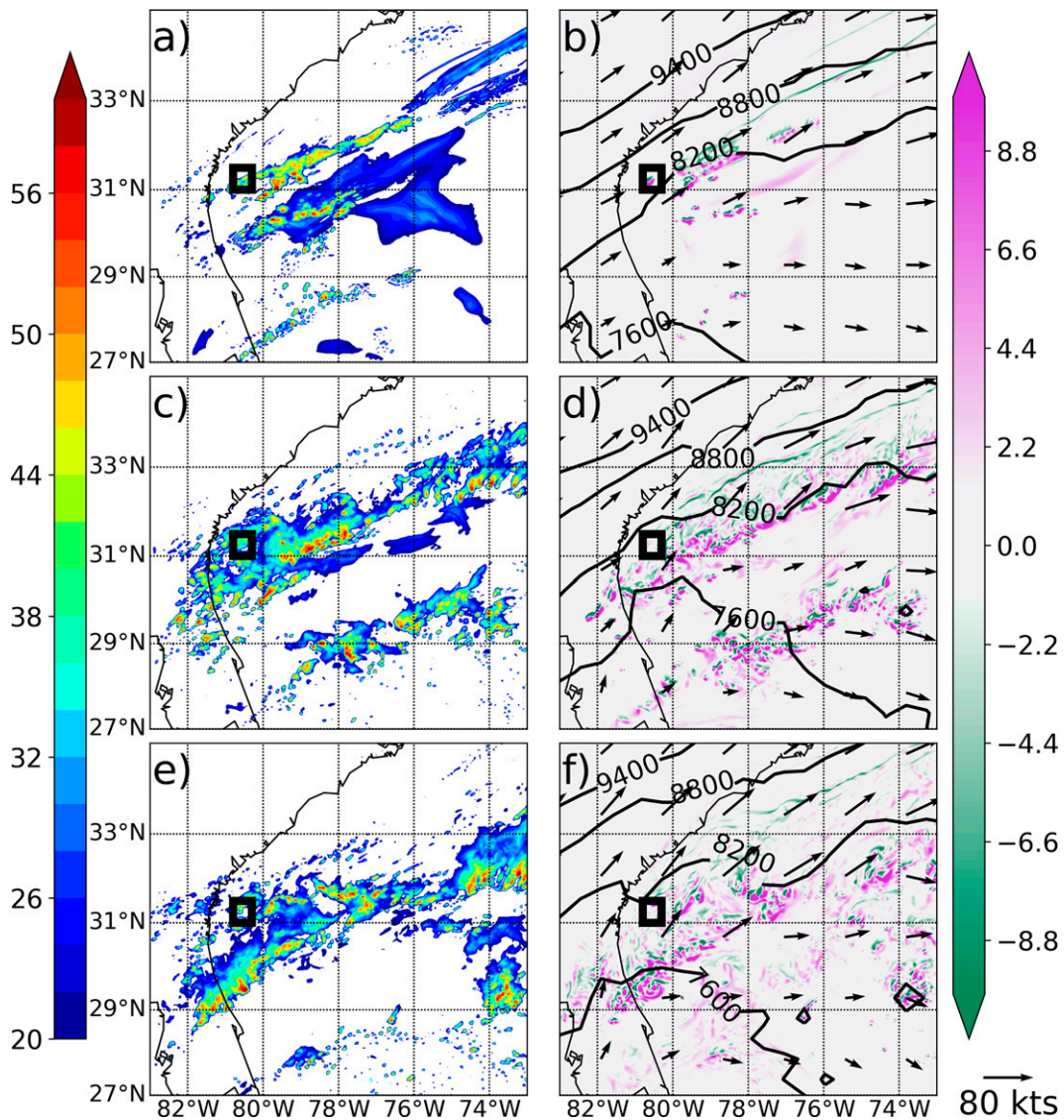


FIG. 6. (a),(c),(e) Simulated composite reflectivity (shaded in dBZ per the color bar at the left) and (b),(d),(f) 335-K geopotential height (black contours every 600 m), 335-K PV (shaded in PVU per the color bar at the right), and 350–320-K vertical wind shear (vectors; kt; reference vector at lower right) at (a),(b) 1500; (c),(d) 1900; and (e),(f) 2300 UTC 9 Sep 2017. The black box denotes the location of the convective cell in Figs. 7 and 8.

however, the simulated TC's loop is somewhat more circular and extends farther to the west (Fig. 5c). Despite these differences, however, the TC Jose lifetime average track error is only 83 km (compared to the climatological 120-h track forecast error of 364 km; Cangialosi 2018), with a lifetime-maximum error of 168 km at 0600 UTC 16 September 2017. Jose's intensity forecast errors were occasionally quite large, with a peak intensity error of nearly 60 kt (31 m s^{-1} ; compared to the climatological 120-h intensity forecast error of 14.3 kt (7.4 m s^{-1}); Cangialosi 2018) near the end of the simulation (Fig. 5d). These large errors are potentially driven by the small size of Jose, with the simulation being unable to depict the sharp horizontal gradients of pressure and wind near the TC's center. The simulated intensity traces still approximately follow the

same trends as what was observed until the last 36 h of the simulation.

4. Convective-scale PV anomalies production and maintenance

The PRE poleward of TC Irma is associated with two major convective bursts, one between 1300 UTC 9 September and 0000 UTC 10 September 2017 (Fig. 6) and another between 0400 and 1300 UTC 10 September 2017 (not shown), within a broader region of predominantly stratiform precipitation. These convective bursts are associated with widespread intense PV dipoles along a baroclinic zone (as inferred from the large vertical wind shear; Figs. 6a,b) extending from

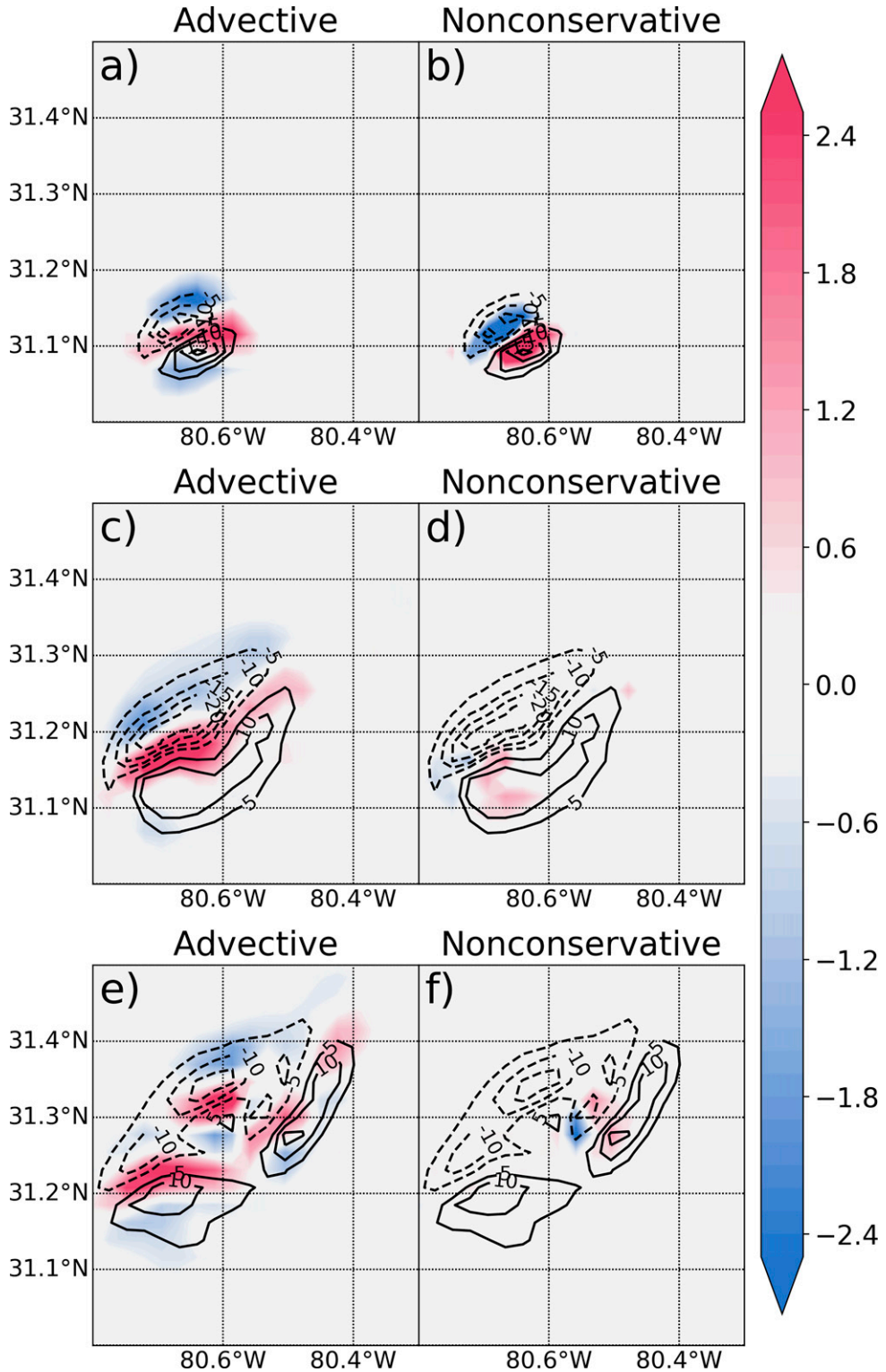


FIG. 7. (a),(c),(e) Three-dimensional advective PV tendency [term 1 on the right-hand side of (3), shaded in PVU min⁻¹ per the color bar at right] and PV (black contours at -20, -15, -10, -5, -2, 2, 5, 10, 15, and 20 PVU) on the 335-K isentropic surface at (a) 1433, (c) 1457, and (e) 1521 UTC 9 Sep 2017. (b),(d),(f) As in (a), (c), and (e), but for the total non-conservative tendency [terms 2 and 3 on the right-hand side of (3)].

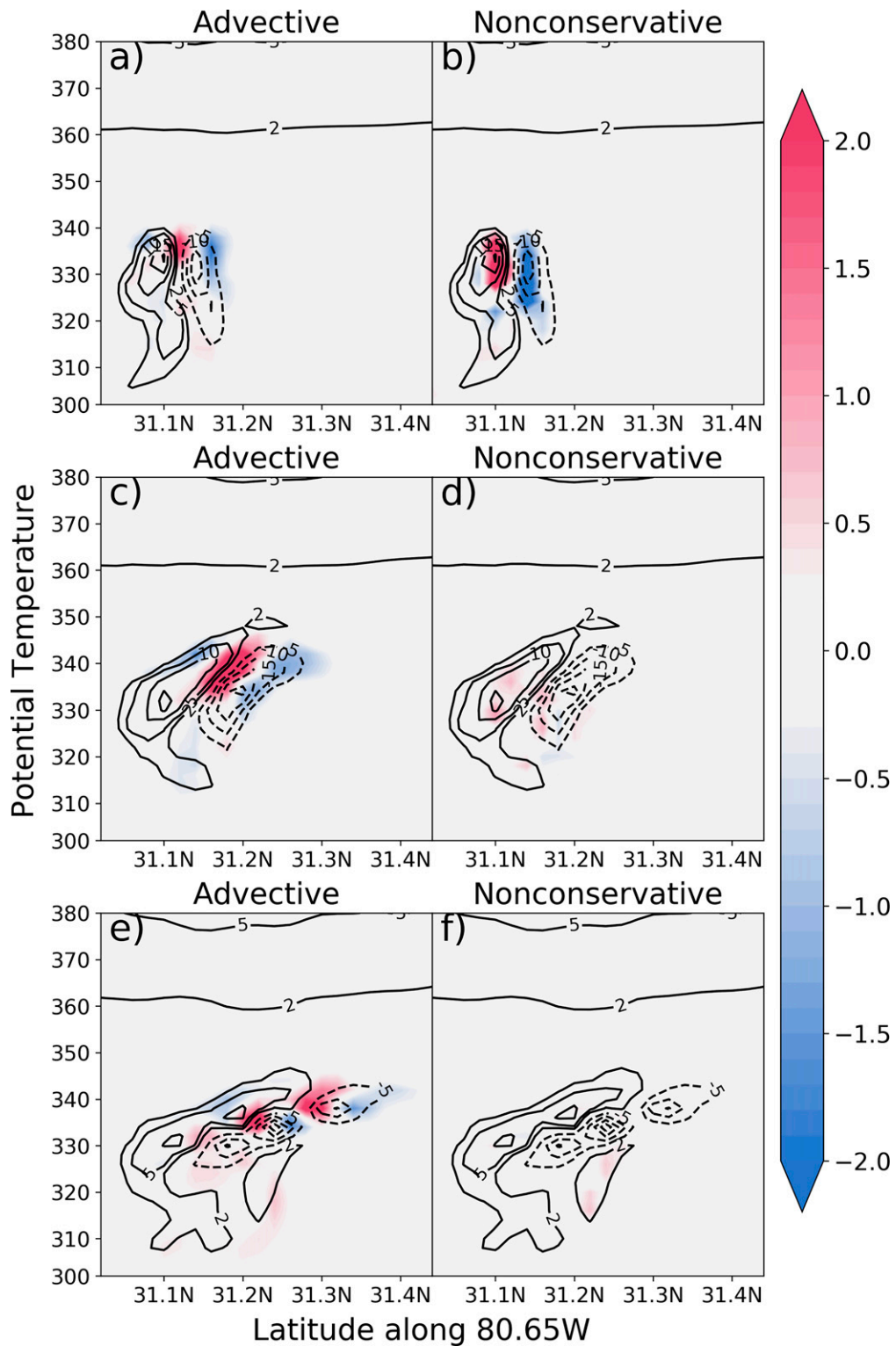


FIG. 8. (a),(c),(e) Vertical cross section [between 300 and 380 K, zonally averaged from 80.8° to 80.3°W (the longitudinal extent of Fig. 7)] between 31° and 31.5°N of the three-dimensional advective PV tendency [term 1 on the right-hand side of (3), shaded in PVU min⁻¹ per the color bar at right] and PV (black contours at -20, -15, -10, -5, -2, 2, 5, 10, 15, and 20 PVU) on the 335-K isentropic surface at (a) 1433, (c) 1457, and (e) 1521 UTC 9 Sep 2017. (b),(d),(f) As in (a), (c), and (e), but for the total non-conservative tendency [terms 2 and 3 on the right-hand side of (3)].

southwest to northeast along the southeastern U.S. coastline. Negative PV is located poleward of the corresponding positive anomalies, which is consistent with the deep-layer vertical wind shear's direction (Figs. 6a,b). Near initiation, while the positive and negative anomalies remain together, the net circulation across the two is roughly equal to zero (not shown), indicating a minimal impact to the surrounding flow. Several hours later, the positive anomalies have largely weakened and/or remained near their initiation locations (Figs. 6c,d), whereas the negative PV becomes elongated and begin to merge into a narrow but long filament (Figs. 6c,d). By 8 h after initiation (Figs. 6e,f), the negative PV continues to persist and has propagated north of their original location immediately offshore from the southeastern U.S. coastline. Altogether, the inertially unstable negative PV persists for multiple hours after initiation. After the negative PV separates from the positive PV, the net circulation over the remaining negative PV is nonzero, thus its impact to the surrounding flow would also be nonzero.

The isentropic PV tendency Eq. (3) is used to diagnose the physical processes by which the PV anomalies initiate, doing so in the context of a representative isolated convective cell embedded within the PRE (Fig. 7). Near initiation, horizontal gradients of microphysical heating dominate the right-hand side of (3), generating a PV dipole on the order of ± 10 PVU in a matter of minutes (Fig. 7b). As this dipole initiates, the background wind field advects the newly generated anomalies, contributing to a nonzero advective tendency (Fig. 7a). These structures extend across an isentropic depth of nearly 30 K (Figs. 8a,b), corresponding to a layer depth of approximately 5000 m (from approximately 5000–10 000 m; not shown). The isolated updraft quickly weakens and tilts downshear, although the PV dipoles persist (Figs. 7c,d and 8c,d). Since microphysical heating is directly tied to ascent, the contributions from the non-conservative tendencies quickly dissipate, leaving the advective tendency as the sole nonnegligible contributor to the total PV tendency (Figs. 7c,d and 8c,d). This process continues forward in time (Figs. 7e,f and 8e,f), with near-zero nonconservative tendencies and nonzero advective tendencies persisting in time. Since the nonconservative tendencies are approximately zero shortly after the PV dipoles' initiation, it is not surprising that the PV anomalies persist for multiple hours (Fig. 6). Over time, the intense localized negative and positive PV slowly weakens due to implicit numerical dampening associated with the WRF-ARW Model's fifth-order-accurate horizontal and third-order-accurate vertical advection schemes (Skamarock et al. 2019; not shown).

5. Local energy flux and the inverse energy cascade

The local energy flux and spectral kinetic energy budget diagnostics introduced in section 2d are each functions of the kinematic field, whereas the PV anomalies detailed in section 4 include both thermodynamic and kinematic structures. As might be expected, however, there is a strong correspondence between PV and kinetic energy anomalies (Fig. 9). PV anomalies directly correspond to absolute-vorticity anomalies (contours in Fig. 9), with a substantial reduction in kinetic energy between the

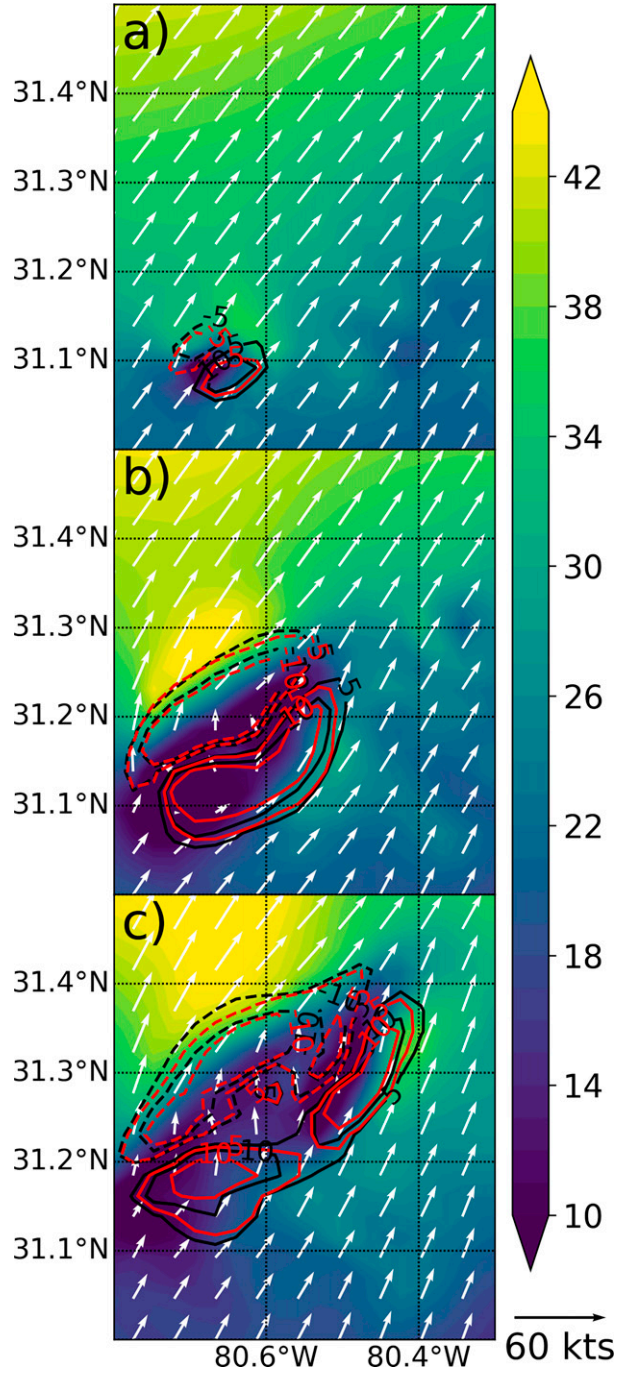


FIG. 9. Horizontal kinetic energy (shaded in 10×10^6 J per the color bar at right), absolute vorticity (black contours at -10 , -5 , 5 , and 10×10^{-4} s^{-1}), horizontal winds (vectors; kt; reference vector at lower right), and PV (red contours at -10 , -5 , 5 , and 10 PVU) on the 335-K isentropic surface at (a) 1433, (c) 1457, and (e) 1521 UTC 9 Sep 2017.

PV/absolute vorticity anomalies (shading in Fig. 9). Between the PV anomalies, the PV anomalies' induced circulations act against the southwesterly background flow, weakening the horizontal wind and thus kinetic energy between them (Fig. 9; Oertel and

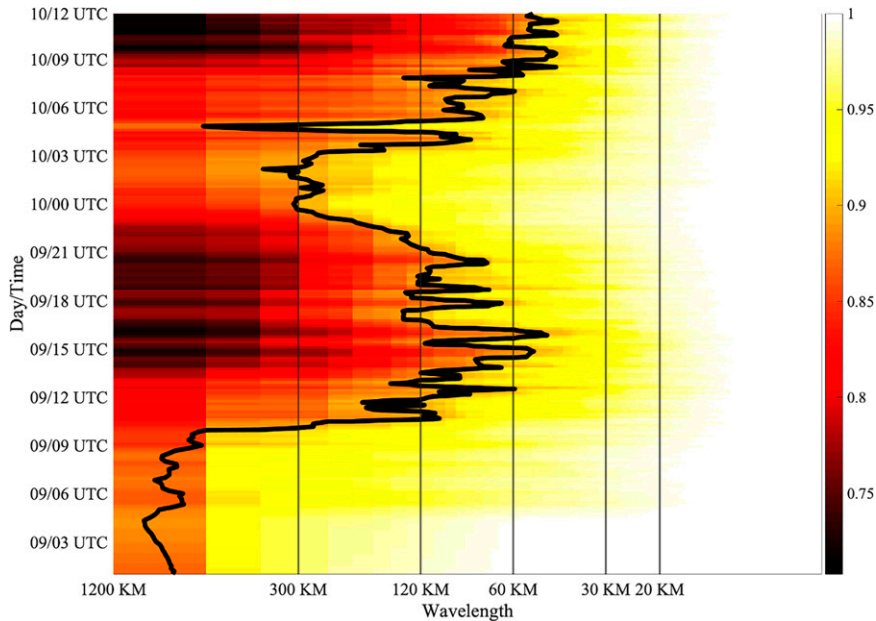


FIG. 10. Cumulative normalized spectral power of area-averaged (28° – 37° N, 89° – 75° W, matching the box in Fig. 1b) absolute vorticity on the 335-K isentropic surface (unitless; shaded per color bar at right). The bold black line denotes the 0.9 (90%) cumulative normalized spectral power contour; i.e., the wavelength above which 90% of the cumulative normalized spectral power is contained.

Schemm 2021). Conversely, poleward of the negative PV anomaly and equatorward of the positive PV anomaly, the horizontal wind and kinetic energy are strengthened by enhancement of the background flow by the circulations' induced flows (Fig. 9c).

Before the convective cells initiate in the PRE and produce regions of convective-scale PV/absolute vorticity, nearly all (~90%–95%) of the spectral power of the absolute vorticity in the vicinity of the PRE is concentrated at the two largest wavelengths (1200 and 600 km; Fig. 10), which is likely driven by the size of the domain and the larger-scales having significantly more energy (not shown). By 0900 UTC 9 September 2017 (9 h into the simulation), the model has sufficiently spun up, which is highlighted by stable behavior from the 90th percentile line (Fig. 10). The percentage of spectral power concentrated at longer wavelengths decreases during the PRE's two convective bursts (from approximately 1300 UTC 9 September to 0000 UTC 10 September 2017 and from 0400 to 1300 UTC 10 September 2017; Fig. 10). The primary increase in power for both convective bursts occur in the range of wavelengths from 300 to 60 km, which is larger than a single convective cell, yet match the approximate size of the clusters of convection identified earlier (Figs. 6 and 10). A reduction of nearly 25% in the total spectral power contribution at the largest wavelengths (from approximately 1300 UTC 9 September to 0000 UTC 10 September 2017 and from 0400 to 1300 UTC 10 September 2017 at $\lambda > 300$ km; Fig. 10) suggests a significant amount of energy which is supplied to mesoscale wavelengths before being transferred upscale and going on to have a nonzero impact to the large-scale flow (Fig. 10).

While the spectral power suggests an increase in energy at meso- α to synoptic scales, it cannot demonstrate whether that energy is being transferred to the large scales, or not. To address this, the local energy flux is calculated in the vicinity of the PRE (Fig. 11). In the sense of the local energy flux, the localized PV, absolute-vorticity, and kinetic-energy anomalies contribute to the u'_ℓ upon which the large-scale strain \bar{u}_ℓ would act. Model-resolved convective cells are associated with positive and negative local energy fluxes (suggestive of forward and inverse energy cascades, respectively) on the meso- γ -scale (Fig. 11a). At convective-scale wavelengths, the small-scale positive and negative regions of the local energy flux largely cancel, causing the mean local energy flux to be closer to zero, albeit with a large amount of temporal variability (Fig. 11e). The local energy flux becomes increasingly negative at larger length scales, suggestive of a broad region of energy cascading from smaller to larger scales (Figs. 11b–d). Area averaging of the local energy flux reveals that at larger wavelengths the temporally and area averaged local energy flux is increasingly negative, demonstrating an inverse cascade of energy up to 1500 km in the vicinity of the PRE (Fig. 11e).

To test the existence of the “thinning” mechanism mentioned earlier, the temporally averaged large-scale strain field in the vicinity of the PRE is calculated (Fig. 12). The environment between TC Irma and the upstream midlatitude trough is characterized by synoptic-scale deformation, with the axis of dilatation (red line in Fig. 12) extending from the southeastern Gulf of Mexico northeastward across Florida and along the Gulf Stream offshore of the southeastern U.S. coastline. Convective cells embedded within the PRE roughly

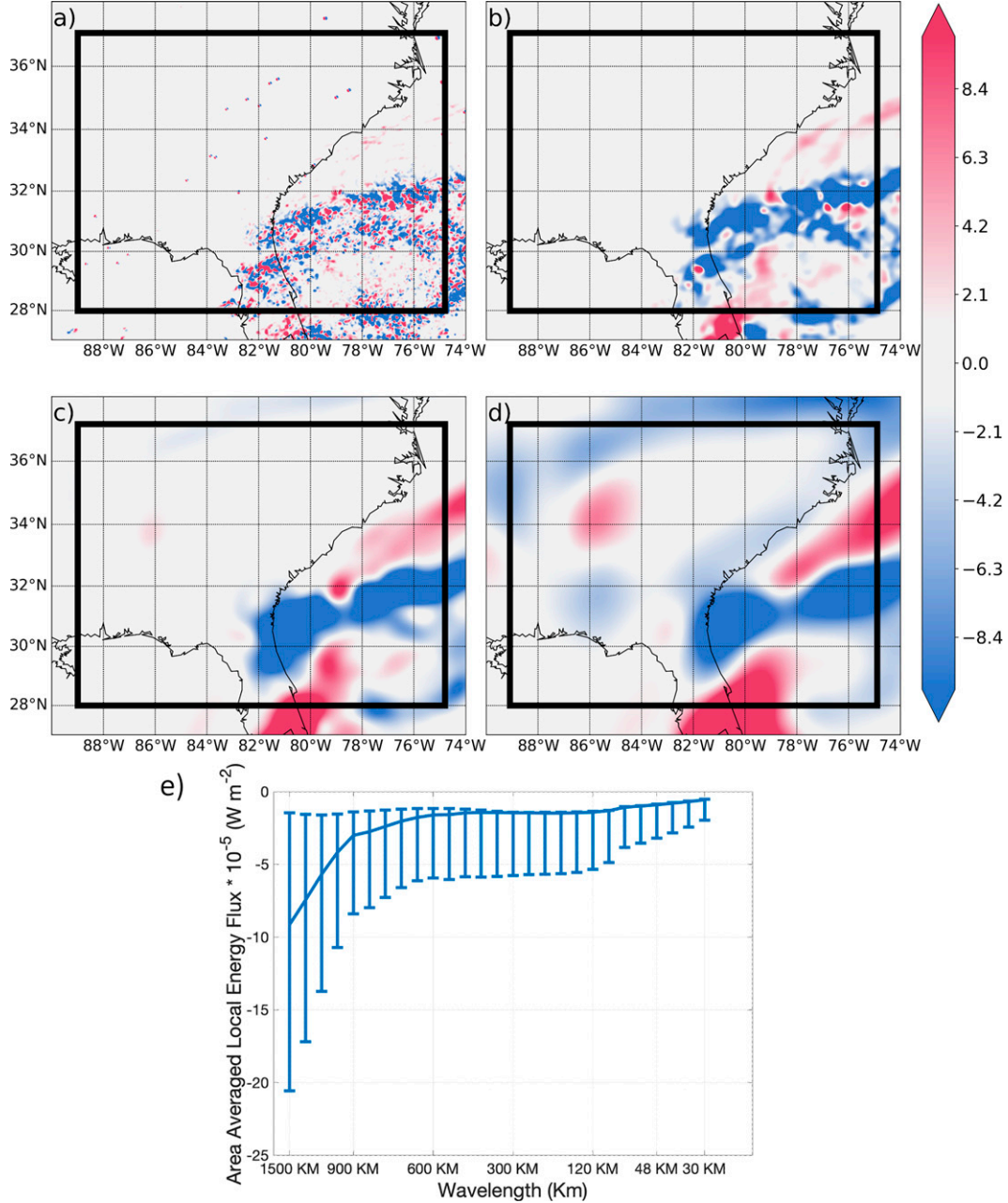


FIG. 11. (a)–(d) Temporally averaged (between 1800 UTC 9 Sep and 1200 UTC 10 Sep 2017) local energy flux (10^{-5} W m^{-2} ; shaded per the color bar at right) on the 335-K isentropic surface for a length scale ℓ of (a) 30, (b) 120, (c) 300, and (d) 600 km. (e) Area- (28° – 37° N, 89° – 75° W, as denoted by the black box that matches the box in Fig. 1b) and temporally (between 1800 UTC 9 Sep and 1200 UTC 10 Sep 2017) averaged local energy flux as a function of length scales between 30 and 1500 km. Error bars in (e) represent the 95th-percentile spread of the area-averaged local energy flux over time.

align with this axis of dilatation, the flow associated with which performs negative work on the turbulent anomalies as it filaments them along the deformation flow (Fig. 12).

The above analyses demonstrate the impacts convective cells have on the local PV and kinetic energy fields and suggest the existence of an inverse cascade of energy in the

vicinity of the PRE. However, they cannot quantify the magnitude of the energy being transferred to large scales or explain the physical processes which transfer this kinetic energy to the upper troposphere. To address these limitations, the kinetic energy framework adopted in Menchaca and Durran (2019) is employed. It is found that convective cell updrafts

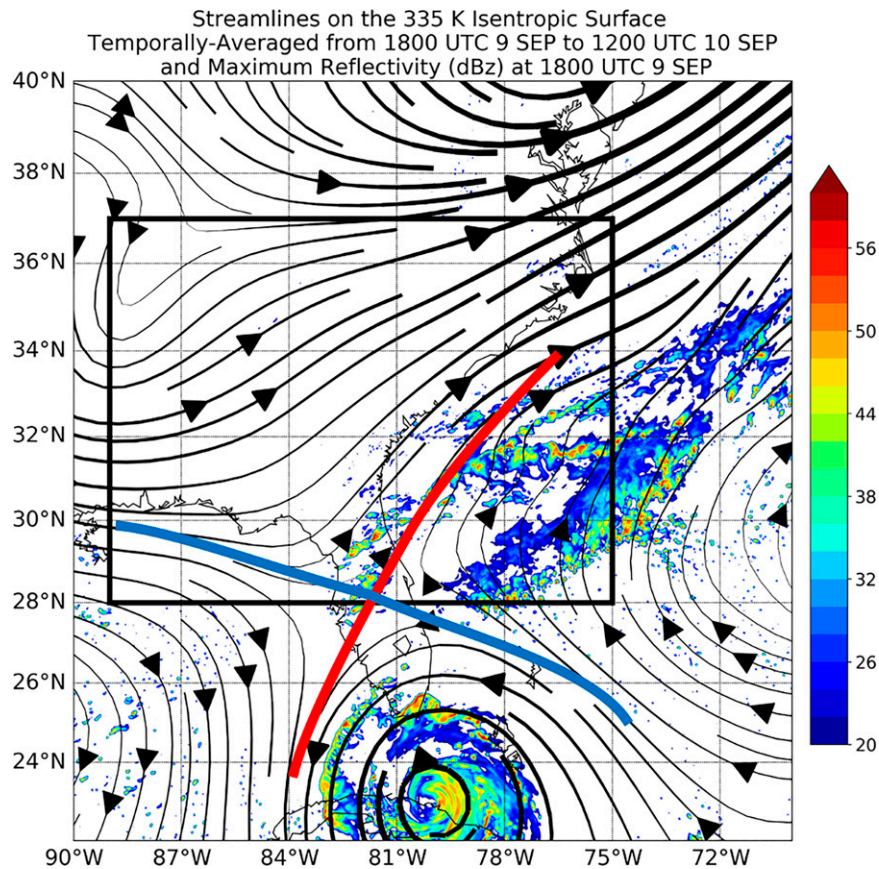


FIG. 12. Streamlines of the temporally averaged (between 1800 UTC 9 Sep and 1200 UTC 10 Sep 2017) large-scale flow \bar{u}_l , where $l = 300$ km, on the 335-K isentropic surface, and simulated composite reflectivity (dBZ; shaded per the color bar at right) at 1800 UTC 9 Sep 2017. The blue line denotes the approximate axis of contraction, and the red line denotes the approximate axis of dilatation, while the black box denotes the region over which area averaging in previous and subsequent analyses are performed that matches the box in Fig. 1b.

inside of the PRE transport (by way of the vertical advective flux) kinetic energy from the lower to the upper troposphere (Figs. 13a,b), whereupon the kinetic energy is transferred upscale by way of an inverse energy cascade (Fig. 13b). This result is insensitive to the precise bounds of the PRE region depicted in Fig. 1b (not shown) and is described in detail in the following two paragraphs.

The midtropospheric [5.5–9 km AGL; encompassing the lower portion of the PV anomalies induced by convection (Fig. 8)] kinetic energy budget in the vicinity of the PRE (black box in Fig. 1b) is characterized by spectral transports and buoyancy forcing that increase kinetic energy and by vertical fluxes and dissipation that decrease kinetic energy (Fig. 13a). Specifically, there is a cascade of energy from large to small scales over all wavelengths ($\Pi_T > 0$; Fig. 13a). The buoyancy force also acts to increase KE from 5.5 to 9 km over all wavelengths ($\partial\Pi_B/\partial k < 0$), which is likely driven by energy supplied by convective updrafts (Fig. 13a). The vertical advective flux, however, extracts energy away from the 5.5–9 km layer at wavelengths of approximately 75 km and larger ($\partial\Pi_V/\partial k > 0$; Fig. 13a), possibly as convective updrafts extract

energy from lower levels. Additionally, the dissipative term acts to decrease KE at nearly all wavelengths and all vertical layers (Figs. 13a–c).

In the mid- to upper troposphere [9.5–13 km AGL; encompassing the upper portion of the PV anomalies induced by convection (Fig. 8)], both the vertical advective and buoyancy fluxes are acting to add KE at nearly all wavelengths ($\partial\Pi_V/\partial k < 0$ and $\partial\Pi_B/\partial k < 0$), suggesting a depositing of energy by convective updrafts at higher levels (Fig. 13b). After being injected into the upper troposphere by convective updraft, the energy concentrated at wavelengths of less than approximately 200 km is cascaded from large to small scales ($\Pi_T > 0$), but for energy at wavelengths greater than or equal to 200 km, there is an inverse cascade to larger wavelengths ($\Pi_T < 0$; Fig. 13b). In the lower stratosphere (13.5–17 km), the vertical advective flux increases KE at all wavelengths (Fig. 13c). Additionally, the buoyancy term has weakened significantly at mesoscale wavelengths, likely due to the rarity of convective updrafts traveling to heights of >15 km (Fig. 13c). The inverse cascade of energy is no longer present and has reversed back to a cascade of energy from large to small scales over all wavelengths (Fig. 13c).

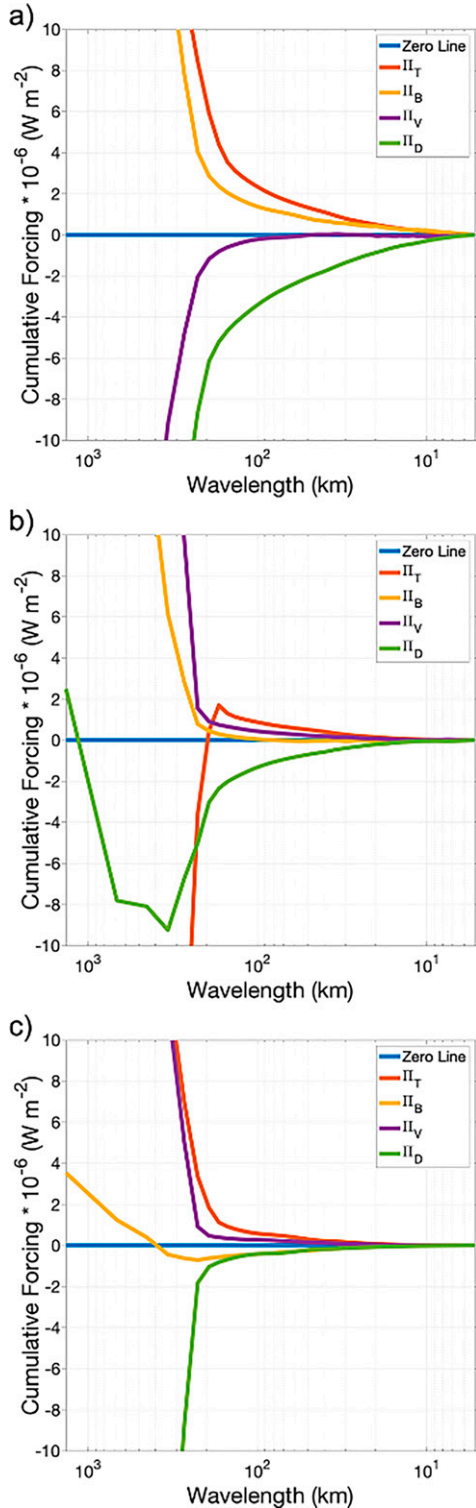


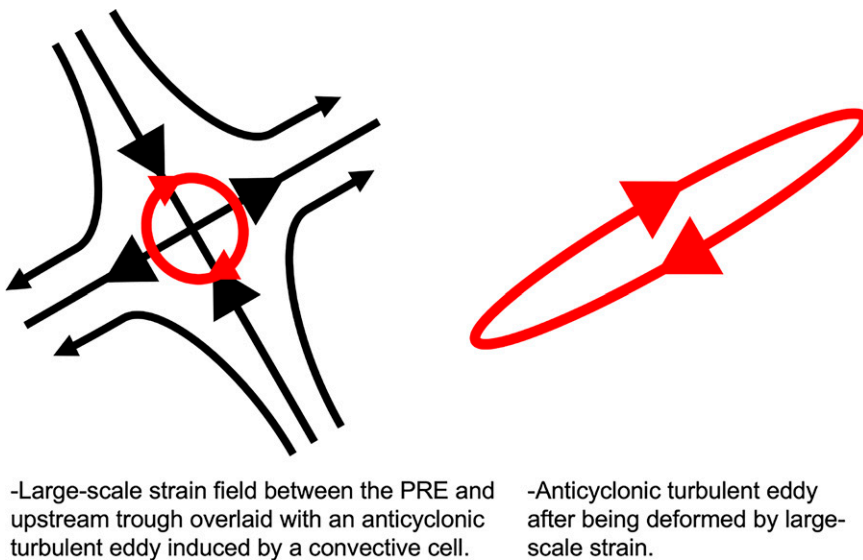
FIG. 13. Cumulative transport (orange line), buoyancy (yellow line), divergence of the vertical kinetic energy flux (purple line), and dissipation (green line) forcing terms in the spectral kinetic energy budget, as calculated over the black box depicted in Fig. 1b, averaged for (a) 5.5–9 km, (b) 9.5–13 km, and (c) 13.5–17 km above ground level, and temporally averaged from 1800 UTC 9 Sep to 1200 UTC 10 Sep 2017.

6. Summary and discussion

Interactions between TCs- and midlatitude troughs are typically conceptualized as being driven by the large-scale, diabatically enhanced vertical redistribution of PV, with the smaller-scale, diabatically enhanced horizontal redistribution of PV typically neglected. However, a separate vein of research has demonstrated the existence of intense convective-scale PV dipoles generated by strong latent heating in deep moist convection. Given that diabatic processes are a potential source of forecast error in TC-trough interactions (Anwender et al. 2008), this study tests the hypothesis that deep, moist convection associated with a PRE modified the synoptic-scale midlatitude waveguide in a recent TC-midlatitude waveguide interaction by way of the production of convective-scale intensely negative PV against the waveguide by deep, moist convection. A convection-allowing simulation of the PRE in advance of North Atlantic TC Irma's (2017) interaction with the midlatitude waveguide is performed to test this hypothesis.

The physical processes that allow for convective-scale PV anomalies to modify the synoptic-scale flow can be conceptualized as follows (Fig. 14). When a convective cell initiates within a vertically sheared flow, its associated horizontal gradients of diabatic heating generate PV anomalies aligned perpendicular to the background vertical wind shear vector, with negative PV to the left of the shear vector and positive PV to the right of the shear vector (Figs. 6 and 7a,b). On the eastern flank of the upstream trough and to the north of Irma, the large-scale strain field can be approximated as having an axis of dilatation oriented from southwest to northeast (Fig. 12). This large-scale strain deforms the convectively generated PV anomalies, stretching them along the axis of dilatation (Figs. 6a,c). The newly deformed PV anomaly covers a larger area than it did before, such that from the circulation theorem its rotation rate must decrease. Due to the alignment of the deformed anomaly with the large-scale strain field, a tensile stress is applied to the large-scale strain, thus reinforcing the large-scale strain, and adding energy to the large-scale flow (Fig. 14). The inverse energy cascade is accomplished by the filamentation of the negative PV (Fig. 14). It is important to note that existence of this inverse cascade of energy is at least partially dependent on the large-scale strain field [Eq. (7)]. Meaning that, even in the absence of convective-scale processes, an inverse cascade of energy may still exist. However, the existence and alignment of the small-scale turbulent eddies with the large-scale strain field in our study likely helps to promote a stronger flux of energy from small to large scales.

This study's results largely support Oertel et al. (2020, 2021) and Oertel and Schemm (2021), each of which demonstrate that convectively generated PV anomalies align perpendicular to the background vertical wind shear vector, the negative PV separates from their positive PV counterparts, and the negative PV subsequently modifies the surrounding flow. The present study builds on these results by identifying an inverse energy cascade in the PRE's vicinity and outlines a physical mechanism by which this cascade is accomplished following methodology presented in Menchaca and Durran (2019).



-Large-scale strain field between the PRE and upstream trough overlaid with an anticyclonic turbulent eddy induced by a convective cell.
-Anticyclonic turbulent eddy after being deformed by large-scale strain.

FIG. 14. Conceptual model demonstrating the impact of large-scale strain (black) on small-scale anticyclonically rotating turbulent eddies (red) such as those convectively generated within a PRE. The cyclonic eddy was neglected as only the anticyclonic eddies propagate northward against the waveguide in our simulation.

While this study identifies a pathway by which convective-scale processes inside of a PRE may modify the large-scale midlatitude pattern, the extent to which the results are generalizable is unclear. This study considers a single numerical simulation of a single case at a single initialization time, and further investigation over a larger sample of cases is warranted to assess the extent to which these findings are representative of all PREs and not just the PRE studied herein. Furthermore, our simulation does not inhibit larger-scale processes from occurring (e.g., large-scale stratiform precipitation) such that it cannot conclusively be said that the PRE's modification of the waveguide is entirely driven by smaller-scale processes and an upscale energy cascade. Therefore, it cannot yet be said how much of the waveguide modification is driven by smaller scales versus how much is driven by larger scales. This study can only demonstrate that the smaller scales can have a larger-scale impacts in this study.

Future studies will test this sensitivity by performing sensitivity analyses in which impacts from convection will be limited/removed by way of piecewise PV inversion (e.g., Grams et al. 2013a,b), or by modifying the diabatic warming in the PRE's vicinity (e.g., turning off diabatic warming in a local area, removing large- and/or small-scale contributions to the diabatic warming). While this study was only applied to a PRE well to the north of Irma, it could be argued that clusters of embedded convection in the outer rainbands of a TC could be viewed in the same fashion. Due to the nature of a TC's rotational wind field, the vertical wind shear vector around the TC would be oriented such that negative PV would always be on the outer radius. One could then view the TC as a feature which "radiates" negative PV, driven by the TC's secondary circulation.

Acknowledgments. The first author of this work was partially supported by a Distinguished Dissertation Fellowship

from the University of Wisconsin–Milwaukee. This research greatly benefited from conversations with and input from Heather Archambault (Citadel), Gary Lackmann (North Carolina State University), Jeff Chagnon (Florida State University), and Sergey Kravtsov (University of Wisconsin–Milwaukee). We would also like to thank Kim Wood (Mississippi State University) for providing plotting assistance with the GOES-16 imagery. The authors thank Editor Christopher Rozoff, and three anonymous reviewers for their thoughtful and detailed suggestions that substantially improved the quality of the work.

Data availability statement. The 0.25° GFS data used to initialize the WRF-ARW simulation in this study are available from <https://rda.ucar.edu/datasets/ds084.1/#description>. The NHC best track and archived forecast data used in this study are available from <https://www.nhc.noaa.gov/data/>. Data relevant to the WRF simulation performed in this study (WPS code, namelists, and input data) can be found on our Zenodo repository at <https://zenodo.org/record/6474366>. GOES-16 imagery data utilized for the animation in the supplementary material are available from <https://aws.amazon.com/public-datasets/goes/>.

REFERENCES

- Anwender, D., P. A. Harr, and S. C. Jones, 2008: Predictability associated with the downstream impacts of the extratropical transition of tropical cyclones: Case studies. *Mon. Wea. Rev.*, **136**, 3226–3247, <https://doi.org/10.1175/2008MWR2249.1>.
- Archambault, H. M., L. F. Bosart, D. Keyser, and J. M. Cordeira, 2013: A climatological analysis of the extratropical flow response to recurring western North Pacific tropical cyclones.

- Mon. Wea. Rev.*, **141**, 2325–2346, <https://doi.org/10.1175/MWR-D-12-00257.1>.
- , D. Keyser, L. F. Bosart, C. A. Davis, and J. M. Cordeira, 2015: A composite perspective of the extratropical flow response recurring western North Pacific tropical cyclones. *Mon. Wea. Rev.*, **143**, 1122–1141, <https://doi.org/10.1175/MWR-D-14-00270.1>.
- Attinger, R., E. Spreitzer, M. Boettcher, H. Wernli, and H. Joos, 2021: Systematic assessment of the diabatic processes that modify low-level potential vorticity in extratropical cyclones. *Wea. Climate Dyn.*, **2**, 1073–1091, <https://doi.org/10.5194/wcd-2-1073-2021>.
- Bloomfield, P., 2000: *Fourier Analysis of Time Series: An Introduction*. 2nd ed. Wiley-Interscience, 288 pp.
- Bosart, L. F., and F. H. Carr, 1978: A case study of excessive rainfall centered around Wellsville, New York, 20–21 June 1972. *Mon. Wea. Rev.*, **106**, 348–362, [https://doi.org/10.1175/1520-0493\(1978\)106<0348:ACSOER>2.0.CO;2](https://doi.org/10.1175/1520-0493(1978)106<0348:ACSOER>2.0.CO;2).
- , and G. M. Lackmann, 1995: Postlandfall tropical cyclone re-intensification in a weakly baroclinic environment: A case study of Hurricane David (September 1979). *Mon. Wea. Rev.*, **123**, 3268–3291, [https://doi.org/10.1175/1520-0493\(1995\)123<3268:PTCRIA>2.0.CO;2](https://doi.org/10.1175/1520-0493(1995)123<3268:PTCRIA>2.0.CO;2).
- , J. M. Cordeira, T. J. Galarneau Jr., B. J. Moore, and H. M. Archambault, 2012: An analysis of multiple predecessor rain events ahead of tropical cyclones Ike and Lowell: 10–15 September 2008. *Mon. Wea. Rev.*, **140**, 1081–1107, <https://doi.org/10.1175/MWR-D-11-00163.1>.
- Cai, M., and M. Mak, 1990: On the basic dynamics of regional cyclogenesis. *J. Atmos. Sci.*, **47**, 1417–1442, [https://doi.org/10.1175/1520-0469\(1990\)047<1417:OTBDOR>2.0.CO;2](https://doi.org/10.1175/1520-0469(1990)047<1417:OTBDOR>2.0.CO;2).
- Cangialosi, J. P., 2018: National Hurricane Center Forecast verification report: 2017 hurricane season. NOAA Tech. Rep., 73 pp., https://www.nhc.noaa.gov/verification/pdfs/Verification_2017.pdf.
- Chagnon, J. M., and S. L. Gray, 2009: Horizontal potential vorticity dipoles on the convective storm scale. *Quart. J. Roy. Meteor. Soc.*, **135**, 1392–1408, <https://doi.org/10.1002/qj.468>.
- Chen, S., R. E. Ecke, G. L. Eyink, M. Rivera, M. Wan, and Z. Xiao, 2006: Physical mechanism of the two-dimensional inverse energy cascade. *Phys. Rev. Lett.*, **96**, 084502, <https://doi.org/10.1103/S0022112008004266>.
- Cordeira, J. M., F. M. Ralph, and B. J. Moore, 2013: The development and evolution of two atmospheric rivers in proximity to western North Pacific tropical cyclones in October 2010. *Mon. Wea. Rev.*, **141**, 4234–4255, <https://doi.org/10.1175/MWR-D-13-00019.1>.
- Cote, M. R., 2007: Predecessor rain events in advance of tropical cyclones. M.S. thesis, Department of Atmospheric and Environmental Sciences, University at Albany, State University of New York, 200 pp.
- Davies-Jones, R. P., 1986: Tornado dynamics. *Thunderstorm Morphology and Dynamics*, 2nd ed. E. Kessler, Ed., University of Oklahoma Press, 197–236.
- Dudhia, J., 1989: Numerical study of convection observed during the Winter Monsoon Experiment using a mesoscale two-dimensional model. *J. Atmos. Sci.*, **46**, 3077–3107, [https://doi.org/10.1175/1520-0469\(1989\)046<3077:NSOCOD>2.0.CO;2](https://doi.org/10.1175/1520-0469(1989)046<3077:NSOCOD>2.0.CO;2).
- Evans, C., and Coauthors, 2017: The extratropical transition of tropical cyclones. Part I: Cyclone evolution and direct impacts. *Mon. Wea. Rev.*, **145**, 4317–4344, <https://doi.org/10.1175/MWR-D-17-0027.1>.
- Eyink, G. J., 2006a: Multi-scale gradient expansion of the turbulent stress tensor. *J. Fluid Mech.*, **549**, 159–190, <https://doi.org/10.1017/S0022112005007895>.
- , 2006b: A turbulent constitutive law for the two-dimensional inverse energy cascade. *J. Fluid Mech.*, **549**, 191–214, <https://doi.org/10.1017/S0022112005007883>.
- Finocchio, P. M., and J. D. Doyle, 2019: How the speed and latitude of the jet stream affect the downstream response to recurring tropical cyclones. *Mon. Wea. Rev.*, **147**, 3261–3281, <https://doi.org/10.1175/MWR-D-19-0049.1>.
- Galarneau, T. J., Jr., 2015: Influence of a predecessor rain event on the track of Tropical Cyclone Isaac (2012). *Mon. Wea. Rev.*, **143**, 3354–3376, <https://doi.org/10.1175/MWR-D-15-0053.1>.
- , L. F. Bosart, and R. S. Schumacher, 2010: Predecessor rain events ahead of tropical cyclones. *Mon. Wea. Rev.*, **138**, 3272–3297, <https://doi.org/10.1175/2010MWR3243.1>.
- Grams, C. M., and H. M. Archambault, 2016: The key role of diabatic outflow in amplifying the midlatitude flow: A representative case study of weather systems surrounding western North Pacific extratropical transition. *Mon. Wea. Rev.*, **144**, 3847–3869, <https://doi.org/10.1175/MWR-D-15-0419.1>.
- , and Coauthors, 2011: The key role of diabatic processes in modifying the upper-tropospheric wave guide: A North Atlantic case-study. *Quart. J. Roy. Meteor. Soc.*, **137**, 2174–2193, <https://doi.org/10.1002/qj.891>.
- , S. C. Jones, C. A. Davis, P. A. Harr, and M. Weissmann, 2013a: The impact of Typhoon Jangmi (2008) on the midlatitude flow. Part I: Upper-level ridgebuilding and modification of the jet. *Quart. J. Roy. Meteor. Soc.*, **139**, 2148–2164, <https://doi.org/10.1002/qj.2091>.
- , —, and —, 2013b: The impact of Typhoon Jangmi (2008) on the midlatitude flow. Part II: Downstream evolution. *Quart. J. Roy. Meteor. Soc.*, **139**, 2165–2180, <https://doi.org/10.1002/qj.2119>.
- Harvey, B., J. Methven, C. Sanchez, and A. Schaefer, 2020: Diabatic generation of negative potential vorticity and its impact on the North Atlantic jet stream. *Quart. J. Roy. Meteor. Soc.*, **146**, 1477–1497, <https://doi.org/10.1002/qj.3747>.
- Hersbach, H., and Coauthors, 2020: The ERA5 global reanalysis. *Quart. J. Roy. Meteor. Soc.*, **146**, 1999–2049, <https://doi.org/10.1002/qj.3803>.
- Hong, S.-Y., J.-H. Kim, J.-O. J. Lim, and J. Dudhia, 2006a: The WRF single-moment 6-class microphysics scheme (WSM6). *J. Korean Meteor. Soc.*, **42**, 129–151.
- , N. Yign, and J. Dudhia, 2006b: A new vertical diffusion package with an explicit treatment of entrainment processes. *Mon. Wea. Rev.*, **134**, 2318–2341, <https://doi.org/10.1175/MWR3199.1>.
- Huffman, G. J., E. F. Stocker, D. T. Bolvin, E. J. Nelkin, and J. Tan, 2019: GPM IMERG Final Precipitation L3 1 day 0.1 degree × 0.1 degree V06 (GPM_3IMERGDF). Goddard Earth Sciences Data and Information Services Center (GES DISC), accessed 16 September 2019, <https://doi.org/10.5067/GPM/IMERGDF/DAY/06>.
- Jiménez, P. A., J. Dudhia, J. F. González-Rouco, J. Navarro, J. P. Montávez, and G.-E. Bustamante, 2012: A revised scheme for the WRF surface layer formulation. *Mon. Wea. Rev.*, **140**, 898–918, <https://doi.org/10.1175/MWR-D-11-00056.1>.
- Keller, J. H., 2017: Amplification of the downstream wave train during extratropical transition: Sensitivity studies. *Mon. Wea. Rev.*, **145**, 1529–1548, <https://doi.org/10.1175/MWR-D-16-0193.1>.

- , and Coauthors, 2019: The extratropical transition of tropical cyclones. Part II: Interaction with the midlatitude flow, downstream impacts, and implications for predictability. *Mon. Wea. Rev.*, **147**, 1077–1106, <https://doi.org/10.1175/MWR-D-17-0329.1>.
- Komaromi, W. A., and J. D. Doyle, 2018: On the dynamics of tropical cyclone and trough interactions. *J. Atmos. Sci.*, **75**, 2687–2709, <https://doi.org/10.1175/JAS-D-17-0272.1>.
- Kraichnan, R. H., 1967: Inertial ranges in two-dimensional turbulence. *Phys. Fluids*, **10**, 1417–1423, <https://doi.org/10.1063/1.1762301>.
- Menchaca, M. O., and D. R. Durran, 2019: The influence of gravity waves on the slope of the kinetic energy spectrum in simulations of idealized midlatitude cyclones. *J. Atmos. Sci.*, **76**, 2103–2122, <https://doi.org/10.1175/JAS-D-18-0329.1>.
- Meneveau, C., and J. Katz, 2000: Scale-invariance and turbulence models for large-eddy simulation. *Annu. Rev. Fluid Mech.*, **32**, 1–32, <https://doi.org/10.1146/annurev.fluid.32.1.1>.
- Mlawer, E. J., S. J. Taubman, P. D. Brown, M. J. Iacono, and S. A. Clough, 1997: Radiative transfer for inhomogeneous atmospheres: RRTM, a validated correlated-k model for the longwave. *J. Geophys. Res.*, **102**, 16 663–16 682, <https://doi.org/10.1029/97JD00237>.
- Moore, B. J., L. F. Bosart, D. Keyser, and M. L. Jurewicz, 2013: Synoptic-scale environments of predecessor rain events occurring east of the Rocky Mountains in association with Atlantic basin tropical cyclones. *Mon. Wea. Rev.*, **141**, 1022–1047, <https://doi.org/10.1175/MWR-D-12-00178.1>.
- National Hurricane Center, 2018: Costliest U.S. tropical cyclones tables updated. NHC Tech. Rep., 3 pp., <https://www.nhc.noaa.gov/news/UpdatedCostliest.pdf>.
- NCEP, 2015: NCEP GFS 0.25 degree global forecast grids historical archive. National Center for Atmospheric Research, Computational and Information Systems Laboratory, accessed 15 October 2018, <https://doi.org/10.5065/D65D8PKW>.
- Oertel, A., and S. Schemm, 2021: Quantifying the circulation induced by convective clouds in kilometer-scale simulations. *Quart. J. Roy. Meteor. Soc.*, **147**, 1752–1766, <https://doi.org/10.1002/qj.3992>.
- , M. Boettcher, H. Joos, M. Sprenger, and H. Wernli, 2020: Potential vorticity structure of embedded convection in a warm conveyor belt and its relevance for large-scale dynamics. *Wea. Climate. Dyn.*, **1**, 127–153, <https://doi.org/10.5194/wcd-1-127-2020>.
- , M. Sprenger, H. Joos, M. Boettcher, H. Konow, M. Hagen, and H. Wernli, 2021: Observations and simulation of intense convection embedded in a warm conveyor belt—How ambient vertical wind shear determines the dynamical impact. *Wea. Climate. Dyn.*, **2**, 89–110, <https://doi.org/10.5194/wcd-2-89-2021>.
- Peng, J., L. Zhang, Y. Luo, and Y. Zhang, 2014: Mesoscale energy spectra of the mei-yu front system. Part I: Kinetic energy spectra. *J. Atmos. Sci.*, **71**, 37–55, <https://doi.org/10.1175/JAS-D-13-085.1>.
- Pohorsky, R., M. Röthlisberger, C. M. Grams, J. Riboldi, and O. Martius, 2019: The climatological impact of recurring North Atlantic tropical cyclones on downstream extreme precipitation events. *Mon. Wea. Rev.*, **147**, 1513–1532, <https://doi.org/10.1175/MWR-D-18-0195.1>.
- Pope, S. B., 2000: *Turbulent Flows*. 1st ed. Cambridge University Press, 802 pp.
- Prince, K. C., and C. Evans, 2020: A climatology of indirect tropical cyclone interactions in the North Atlantic and western North Pacific basins. *Mon. Wea. Rev.*, **148**, 4035–4059, <https://doi.org/10.1175/MWR-D-19-0377.1>.
- Quinting, J. F., and S. C. Jones, 2016: On the impact of tropical cyclones on Rossby wave packets: A climatological perspective. *Mon. Wea. Rev.*, **144**, 2021–2048, <https://doi.org/10.1175/MWR-D-14-00298.1>.
- Riboldi, J., C. M. Grams, M. Riemer, and H. M. Archambault, 2019: A phase locking perspective on Rossby wave amplification and atmospheric blocking downstream of recurring western North Pacific tropical cyclones. *Mon. Wea. Rev.*, **147**, 567–589, <https://doi.org/10.1175/MWR-D-18-0271.1>.
- Riemer, M., and S. C. Jones, 2010: The downstream impact of tropical cyclones on a developing baroclinic wave in idealized scenarios of extratropical transition. *Quart. J. Roy. Meteor. Soc.*, **136**, 617–637, <https://doi.org/10.1002/qj.605>.
- , —, 2014: Interaction of a tropical cyclone with a high-amplitude, midlatitude wave pattern: Waviness analysis, trough deformation, and track bifurcation. *Quart. J. Roy. Meteor. Soc.*, **140**, 1362–1376, <https://doi.org/10.1002/qj.2221>.
- , —, and C. A. Davis, 2008: The impact of extratropical transition on the downstream flow: An idealized modeling study with a straight jet. *Quart. J. Roy. Meteor. Soc.*, **134**, 69–91, <https://doi.org/10.1002/qj.189>.
- Rios-Berrios, R., R. D. Torn, and C. A. Davis, 2016: An ensemble approach to investigate tropical cyclone intensification in sheared environments. Part I: Katia (2011). *J. Atmos. Sci.*, **73**, 71–93, <https://doi.org/10.1175/JAS-D-15-0052.1>.
- Riviére, G., and A. Joly, 2006: Role of the low-frequency deformation field on the explosive growth of extratropical cyclones at the jet exit. Part I: Barotropic critical region. *J. Atmos. Sci.*, **63**, 1965–1981, <https://doi.org/10.1175/JAS3728.1>.
- Skamarock, W. C., and Coauthors, 2019: A description of the Advanced Research WRF Model version 4. NCAR Tech. Note NCAR/TN-556+STR, 145 pp., <https://doi.org/10.5065/1dfh-6p97>.
- Tewari, M., and Coauthors, 2004: Implementation and verification of the unified Noah land surface model in the WRF model. *20th Conf. on Weather Analysis and Forecasting/16th Conf. on Numerical Weather Prediction*, Seattle, WA, Amer. Meteor. Soc., 14.2A, https://ams.confex.com/ams/84Annual/techprogram/paper_69061.htm.
- Torn, R. D., and C. A. Davis, 2012: The influence of shallow convection on tropical cyclone track forecasts. *Mon. Wea. Rev.*, **140**, 2188–2197, <https://doi.org/10.1175/MWR-D-11-00246.1>.
- , and G. J. Hakim, 2015: Comparison of wave packets associated with extratropical transition and winter cyclones. *Mon. Wea. Rev.*, **143**, 1782–1803, <https://doi.org/10.1175/MWR-D-14-00006.1>.
- Velden, C. S., and L. M. Leslie, 1991: The basic relationship between tropical cyclone intensity and the depth of the environmental steering layer in the Australian region. *Wea. Forecasting*, **6**, 244–253, [https://doi.org/10.1175/1520-0434\(1991\)006<0244:TBRBTC>2.0.CO;2](https://doi.org/10.1175/1520-0434(1991)006<0244:TBRBTC>2.0.CO;2).
- Virtanen, P., and Coauthors, 2020: SciPy 1.0: Fundamental algorithms for scientific computing in python. *Nat. Methods*, **17**, 261–272, <https://doi.org/10.1038/s41592-019-0686-2>.
- Xiao, Z., M. Wan, S. Chen, and G. Eyink, 2009: Physical mechanism of the inverse energy cascade of two-dimensional turbulence: A numerical investigation. *J. Fluid Mech.*, **619**, 1–44, <https://doi.org/10.1017/S0022112008004266>.
- Zhang, C., and Y. Wang, 2017: Projected future changes of tropical cyclone activity over the western north and south Pacific in a 20-km-mesh regional climate model. *J. Climate*, **30**, 5923–5941, <https://doi.org/10.1175/JCLI-D-16-0597.1>.